Editors' Suggestion

Viscosity of pure-glue QCD from the lattice

Luis Altenkort,[1] Alexander M. Eller,[2] Anthony Francis,[3] Olaf Kaczmarek,[1] Lukas Mazur,[4] Guy D. Moore,[2] and Hai-Tao Shu[5,*]

[1]*Fakultät für Physik, Universität Bielefeld, D-33615 Bielefeld, Germany*
[2]*Institut für Kernphysik, Technische Universität Darmstadt Schlossgartenstraße 2, D-64289 Darmstadt, Germany*
[3]*Institute of Physics, National Yang Ming Chiao Tung University, 30010 Hsinchu, Taiwan*
[4]*Paderborn Center for Parallel Computing, Paderborn University, D-33098 Paderborn, Germany*
[5]*Institut für Theoretische Physik, Universität Regensburg, D-93040 Regensburg, Germany*

(Received 28 November 2022; accepted 22 June 2023; published 11 July 2023)

We calculate shear viscosity and bulk viscosity in $SU(3)$ gauge theory on the lattice at $1.5T_c$. The viscosities are extracted via a Kubo formula from the reconstructed spectral function which we determine from the Euclidean time dependence of the corresponding channel of the energy-momentum tensor correlators. We obtain unprecedented precision for the correlators by applying gradient-flow and blocking methods. The correlators are extrapolated to the continuum and then to zero-flow time. To extract the viscosities we fit theoretically inspired models to the lattice data and cross-check the fit results using the Backus-Gilbert method. The final estimates for shear and bulk viscosity are $\eta/s = 0.15$–0.48 and $\zeta/s = 0.017$–0.059.

DOI: 10.1103/PhysRevD.108.014503

I. INTRODUCTION

The shear viscosity η and bulk viscosity ζ of the hot quark-gluon plasma characterize the dissipation which occurs due to nonuniform flow, such as occurs in heavy ion collisions. They have been a topic of intense study for the last two decades. Experimental results [1–5] suggest a small shear viscosity; indeed, based on the determined values of elliptic and higher-order flow as functions of momentum and impact parameter, the best extractions of the shear viscosity are in the range $1/(4\pi) < \eta/s < 2/(4\pi)$ [6]. This is close to the claimed lower bound on η/s obtained from $\mathcal{N} = 4$ supersymmetric Yang-Mills theory at strong coupling, which predicts $\eta/s = 1/(4\pi)$ [7]. While leading-order weak-coupling calculations [8,9], extrapolated to the physical coupling strength, suggest a larger shear viscosity $\eta/s \sim 0.5$–1, the next-to-leading correction to this result at a physically interesting coupling and temperature reduces the tension, implying $\eta/s \sim 0.2$ [10]. The size of this difference implies that the perturbative series shows poor convergence. As for the bulk viscosity, its extraction from experiments shows that it is nonzero but somewhat smaller than the shear viscosity at temperatures of order 200 MeV [6]. At higher temperatures we have a leading-order perturbative calculation [11] which shows that, for $0.06 < \alpha_s < 0.3$, $\zeta/s \sim 0.02\alpha_s^2$. That is, as the theory becomes more conformal at higher temperatures, the bulk viscosity is expected to become small, but it can nevertheless play a role at lower temperatures where QCD behaves strongly nonconformally.

We want a first-principles theoretical determinations of shear and bulk viscosity, to accompany the values extracted from experiment. The temperatures achieved in real-world heavy ion collisions are in a range where perturbation theory does not appear to be applicable, and so truly nonperturbative methods are needed. Our best first-principles nonperturbative tool is lattice gauge theory, which we will pursue in this work. Like previous literature, we will work within pure $SU(3)$ gauge theory, but one focus of our work is to develop tools which will be straightforward to extend to the theory with dynamical quarks.

The pioneering works [12–14] established the general approach for investigating shear viscosity via unequal Euclidean-time, zero space-momentum energy-momentum tensor (EMT) correlation functions. More recent studies [15,16] have extended this work to consider a range of temperatures. However, these works used rather coarse and small lattices, meaning that cutoff effects may be severe. Recently, a lattice calculation using the gradient flow method was conducted on a $64^3 \times 16$ lattice [17].

*Corresponding author.
hai-tao.shu@ur.de

In that work, the shear viscosity is extracted at finite flow time, making the results difficult to interpret [18].

The standard way to investigate transport coefficients on the lattice is through Kubo formulas, which relate these coefficients to spectral functions, which in turn are related to Euclidean correlators through analytic continuation. The biggest challenge is that the energy-momentum tensor correlators, from which the viscosities are extracted, are extremely noisy, such that a noise-reduction technique must be employed to obtain the necessary precision. In Refs. [14,16] the multilevel algorithm [19] was used; in this work we instead make use of the gradient-flow method [20–23] and the blocking method [24] which we proposed recently. In comparison to multilevel algorithms, the gradient flow approach has the advantages that it is straightforward to apply to the full theory with dynamical quarks, and it helps with the problem of operator renormalization. This paves the way for a future study in full QCD. The signal is improved further via the blocking method, up to a factor of 7 without additional computation cost, as we demonstrate in [24]. With these two methods we are able to achieve high precision for the desired correlators.

Our lattice setup consists of five large and fine lattices, of which the coarsest one ($64^3 \times 16$) is already as large as the finest lattice used in previous literature. The largest and finest lattice in our study is of size $144^3 \times 36$ at $\beta = 7.544$ ($a = 0.0117$ fm). With our setup, including such a fine lattice, the continuum extrapolation is well-behaved and, thanks to the large temporal extents of the underlying lattices, the results of the spectral reconstruction will be more reliable.

In the following we will start with the definition of the EMT under gradient flow and explain how shear and bulk viscosity can be obtained from the EMT correlators. In Sec. III we give the lattice setup used in this study. Sec. IV is devoted to the nonperturbative renormalization of the EMT correlators. After a short illustration to the temperature-correction and tree-level improvement in Sec. V we continue with the discussions of continuum extrapolation and flow-time extrapolation in Sec. VI. In Sec. VII we focus on the extraction of viscosities via spectral analysis and provide our estimates for the viscosities. The conclusion is given in Sec. VIII.

II. TRANSPORT, ENERGY-MOMENTUM TENSOR, AND GRADIENT FLOW

The fundamental object of our study is the energy-momentum tensor $T_{\mu\nu}$, defined as the Noether current of 4-translation symmetry (or equivalently as the variation of the action with respect to the spacetime metric). Shear viscosity is the response of T_{ij} to shear flow, under which the traceless part of $\partial_i v_j$ is nonzero. Shear flow also couples to the energy-momentum tensor, so the Kubo relation describing the shear viscosity involves a correlation function of two traceless energy-momentum tensors,

$$\eta(T) = \lim_{\omega\to 0} \frac{\rho_{\text{shear}}(\omega, T)}{\omega}, \tag{1}$$

$$\rho_{\text{shear}}(\omega, T) = \frac{1}{10}\int \mathrm{d}^3x \mathrm{d}t\, e^{i\omega t}\langle[\pi_{ij}(x,t), \pi_{ij}(0,0)]\rangle,$$
$$\pi_{ij} = T_{ij} - \frac{1}{3}\delta_{ij}T_{kk}. \tag{2}$$

Similarly, bulk viscosity is the response of the trace of the energy-momentum tensor to a divergent fluid flow, which also couples to the trace of the energy-momentum tensor,

$$\zeta(T) = \frac{1}{9}\lim_{\omega\to 0} \frac{\rho_{\text{bulk}}(\omega, T)}{\omega}, \tag{3}$$

$$\rho_{\text{bulk}} = \int \mathrm{d}^3x \mathrm{d}t\, e^{i\omega t}\langle[T_{\mu\mu}(x,t), T_{\nu\nu}(0,0)]\rangle. \tag{4}$$

Our approach will be to use analyticity to relate these spectral functions to the Euclidean, time-dependent correlation (still at zero momentum or equivalently with $\int \mathrm{d}^3x$),

$$G(\tau) = \int_0^\infty \frac{\mathrm{d}\omega}{\pi} \frac{\cosh[\omega(1/2T - \tau)]}{\sinh(\omega/2T)} \rho(\omega, T). \tag{5}$$

This expression can in principle be inverted to determine the spectral function, a task we will return to in Sec. VIII. Here $G(\tau)$ is the Euclidean function associated to the respective spectral function, that is,

$$G_{\text{shear}}(\tau) = \frac{1}{10}\int \mathrm{d}^3x \langle \pi_{ij}(0,\vec{0})\pi_{ij}(\tau,\vec{x})\rangle,$$
$$G_{\text{bulk}}(\tau) = \int \mathrm{d}^3x \langle T_{\mu\mu}(0,\vec{0})T_{\mu\mu}(\tau,\vec{x})\rangle. \tag{6}$$

Our main task will be evaluating the continuum limit of these correlation functions precisely.

There are two principle challenges when treating energy-momentum tensor correlations on the lattice; the correlations are very noisy, and because of the lack of continuous translation symmetry on the lattice, there is no obvious choice for the energy-momentum tensor operator. In particular, different components of π_{ij} renormalize differently, which presents a challenge. Both problems are ameliorated if we utilize gradient flow to generate our energy-momentum operators. Gradient flow is defined as the iterative replacement of the gauge fields $A_\mu(x)$ with fields containing less UV fluctuations, $B_\mu(x, \tau_{\text{F}})$, through the definitions [20]

$$B_\nu(x,\tau_F=0)=A_\nu(x),$$
$$\dot{B}_\mu = D_\nu G_{\nu\mu},$$
$$G_{\mu\nu}=\partial_\mu B_\nu-\partial_\nu B_\mu+[B_\mu,B_\nu],$$
$$D_\mu=\partial_\mu+[B_\mu,\cdot]. \quad (7)$$

That is, at $\tau_F=0$ the flowed field is the nonflowed field, but the field then evolves under a covariant heat equation which iteratively removes the most UV fluctuations of the field. Using the flowed field to construct operators such as the energy-momentum tensor leads to operators with well behaved renormalization properties and improved rotational invariance. In terms of the gradient-flowed field, we define the gradient-flowed squared field strength operator and the traceless tensor operator as

$$E(\tau_F,x)=\frac{1}{4}F^a_{\rho\sigma}(x,\tau_F)F^a_{\rho\sigma}(x,\tau_F),$$
$$U_{\mu\nu}(x,\tau_F)=F^a_{\mu\rho}(x,\tau_F)F^a_{\nu\rho}(x,\tau_F)-\delta_{\mu\nu}E(\tau_F,x). \quad (8)$$

The energy-momentum tensor can then be written in terms of these two operators and two not yet known coefficients as [25]

$$T_{\mu\nu}(\tau_F,x)=c_1(\tau_F)U_{\mu\nu}(\tau_F,x)+4c_2(\tau_F)\delta_{\mu\nu}E(\tau_F,x). \quad (9)$$

Here c_1, c_2 are the coefficients on the traceless and pure-trace parts of the tensor, respectively. Arguably one should perform a vacuum subtraction from $E(\tau_F,x)$, but in practice we always compute connected correlation functions, which implements such a subtraction automatically.

There are two approaches to determining the coefficients $c_1,c_2(\tau_F)$. Suzuki has determined them up to 2-loop and 3-loop order in the $\overline{\text{MS}}$-scheme [26]:

$$c_1^{(\text{N}^2\text{LO})}(\tau_F)=\frac{1}{g^2(\mu)}\sum_{n=0}^{2}k_1^{(n)}(L(\mu,\tau_F))\left[\frac{g^2(\mu)}{(4\pi)^2}\right]^n, \quad (10)$$

$$c_2^{(\text{N}^3\text{LO})}(\tau_F)=\frac{1}{g^2(\mu)}\sum_{n=1}^{4}k_2^{(n)}(L(\mu,\tau_F))\left[\frac{g^2(\mu)}{(4\pi)^2}\right]^n, \quad (11)$$

where the coefficients $k_1^{(n)}$, $k_2^{(n)}$ can be found in [27,28]. Here $L(\mu,\tau_F)\equiv\log(2\mu^2e^{\gamma_E}\tau_F)$ and the running coupling can be evaluated in the $\overline{\text{MS}}$-scheme at scale $\mu=1/\sqrt{8\tau_F}$ [29]. The series for c_2 begins with a constant and is known to one higher order than for c_1; therefore it suffers very little coupling and renormalization-point uncertainty, and is more accurate than any numerics-based nonperturbative estimate which we could develop. Therefore, we use the series expansion for c_2. The error in this series expansion is negligible, below 0.1%. This will be swamped by statistical errors in our correlation functions and will play no role in our error analysis.

In contrast, since c_1 depends on the coupling at leading order, the use of a series expansion is significantly less reliable. Instead, we will perform a nonperturbative renormalization on the lattice in Sec. IV, based on ideas developed by Giusti and Pepe [30].

According to small-flow time expansion [31], any composite operator at finite flow time can be expressed as superposition of renormalized operators with finite, flow-dependent coefficients [32]. That is, one can expand our stress-tensor operator in an operator product expansion, where the first term is the desired stress tensor and higher terms represent various higher-dimension operators with coefficients containing positive powers of τ_F. Therefore, one expects that the correlation functions we evaluate, at separation τ, correspond to the correct correlation functions, plus corrections which appear as a series expansion in (τ_F/τ^2). Determining the desired correlation function therefore requires an extrapolation to $\tau_F\to 0$ to eliminate the effects of these high-dimension contaminants. Only some finite range of τ_F values will actually be useful in this extrapolation; larger values of τ_F, such that (τ_F/τ^2) is not small, will be outside of the range where an extrapolation is possible. Solving Eq. (7) perturbatively suggests that the flow smears the gauge field with a radius $r\simeq\sqrt{8\tau_F}$ [20]. In general this radius should be larger than one lattice spacing to suppress the lattice effects and noise, and at the same time smaller than half the lattice extent so that the flow radius does not interact with the lattice periodicity. For a specific operator there can be further constraints on the flow radius. How much flow can be applied and what Ansatz should be used for the $\tau_F\to 0$ extrapolation will be discussed in a later section.

III. LATTICE SETUP

Our lattice calculations are carried out in $SU(3)$ Yang-Mills theory in four-dimensional spacetime with periodic boundary conditions for all directions. We summarize the settings in Table I. The gauge configurations are generated using the standard Wilson gauge action on five large, fine, isotropic lattices. On each lattice we generate 10,000 configurations. To ensure the gauge fields are fully thermalized the first 4,000 sweeps (each consists of one heat bath and four over-relaxation steps) are discarded. In the sampling procedure the configurations are stored after

TABLE I. β values, lattice spacings, lattice sizes, blocking bin size n_σ and number of configurations in this study.

a (fm)	a^{-1} (GeV)	N_σ	n_σ	N_τ	β	T/T_c	#Configuration
0.0262	7.534	64	4	16	6.8736	1.5104	10000
0.0215	9.187	80	4	20	7.0350	1.4734	10000
0.0178	11.11	96	4	24	7.1920	1.4848	10000
0.0140	14.14	120	6	30	7.3940	1.5118	10000
0.0117	16.88	144	8	36	7.5440	1.5042	10000

every 500 sweeps. This removes the autocorrelations in observables as we have confirmed. All the lattices are set to the same temperature $\sim 1.5 T_c$ by tuning the β value. The scale is set via the Sommer parameter r_0 [33] with state-of-the-art value $r_0 T_c = 0.7457$ [34]. The parametrization form needed in scale setting is taken from [34] with updated coefficients from [35].

We use the clover definition of the energy-momentum tensor appearing in Eq. (8). The gradient flow is a Symanzik improved version [36]. We measure the EMT correlators at 140 discrete flow times in the range $\sqrt{8\tau_F} T \in \{0.004, \ldots, 0.375\}$ using an adaptive step-size method. In this method the step size is updated after each integration step such that the error in the integration does not exceed a certain tolerance [37]. The bin size used in the blocking method is given as n_σ in Table I.

IV. RENORMALIZATION

In this section we describe how we determine the renormalization constants appearing in Eq. (9). We determine the constant c_1 using a method inspired by the work of Giusti and Pepe [30]. Namely, we observe that the enthalpy density is given by

$$\langle \epsilon + P \rangle_{\tau_F} = c_1(\tau_F) \left\langle \frac{1}{3} U_{ii}(\tau_F) - U_{00}(\tau_F) \right\rangle, \quad (12)$$

where "0" denotes the time direction. Since $\epsilon + P$ has been measured at the subpercent level [38], we can determine c_1 through the ratio $c_1(\tau_F) = \langle \epsilon + P \rangle_{\tau_F} / \langle \frac{1}{3} U_{ii}(\tau_F) - U_{00}(\tau_F) \rangle$. We will explain below why this also determines the coefficients for the off-diagonal components of the stress tensor, to sufficient precision for this work.

Unfortunately the enthalpy density is proportional to T^4 and therefore to N_τ^{-4}, which leads to a poor signal-to-noise ratio for the finest lattices. We overcome this limitation by measuring $\epsilon + P$ at a range of N_τ values listed in Table II, not just the ones given in Table I. This is possible because the renormalization constant c_1 depends on the lattice spacing but not on the temperature. However, after enough gradient flow, the gradient flow radius starts to interact with the periodicity radius and the result becomes contaminated and unreliable. A leading-order perturbative estimate of this effect is that [39]

$$\frac{\langle \frac{1}{3} U_{ii} - U_{00} \rangle_{\text{flowed}}}{\langle \frac{1}{3} U_{ii} - U_{00} \rangle_{\text{true}}} = 1 - \frac{180}{\pi^4} e^{-1/x} \left(1 + \frac{1}{x} + \frac{1}{2x^2} \right), \quad \text{with} \quad x = 8\tau_F T^2. \quad (13)$$

We illustrate the method, and the effect of the different N_τ choices, in Fig. 1, which shows c_1 for our finest lattice at different temperatures. It can be seen that, at very small flow times c_1, measurements from different temperatures agree with each other, with smaller statistical errors for the smaller N_τ values. With increasing flow time, the higher-temperature c_1 values start to deviate from the lower ones. The point where Eq. (13) implies a 1% correction is marked for each N_τ value by a vertical bar, and it corresponds well with the flow time value where a given lattice starts to deviate clearly from the larger-N_τ lattices.

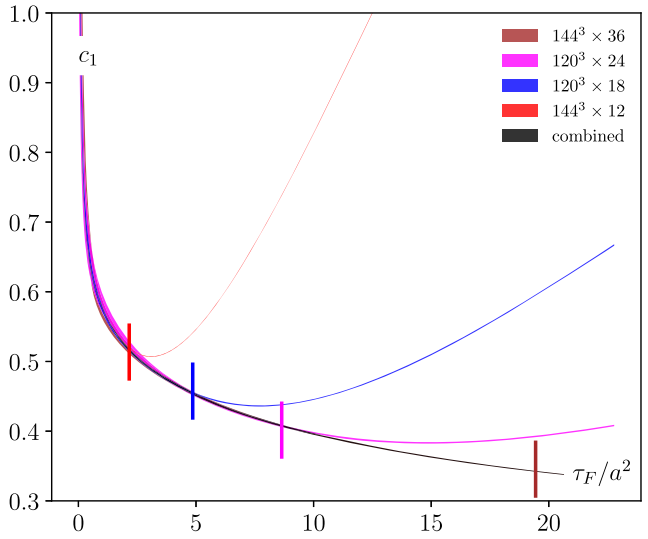

FIG. 1. c_1 measured at several higher temperatures at $\beta = 7.544$ and their weighted average. The vertical bars indicate the flow depth where each N_τ choice is expected to become unreliable.

Our final estimate for c_1 will be based on a weighted average of the value determined from each N_τ value we explored. The weight is determined as $1/(\sigma_{\text{stat}} + \sigma_{\text{syst}})^2$ where σ_{stat} is the statistical uncertainty from the lattice data and σ_{syst} is the systematic shift as determined from Eq. (13). The averaged c_1 is the black curve labeled "combined" in Fig. 1.

We repeat this procedure for the other lattice spacings and summarize the final c_1 in Fig. 2. The statistical error in c_1 is small, ranging from 1.1% at the smallest flow time we use to 0.27% at the largest flow time we use. A table presenting the statistical uncertainties of c_1 at each lattice spacing for a range of flow times is provided in Appendix A.

Let us now focus on the small flow-time region, to establish how much flow time is enough to eliminate lattice spacing effects. We have added one more, still finer lattice ($\beta = 7.793$, with $N_\tau = 48$ when $T/T_c = 1.5$) so that we can compare to a still more continuumlike case. We can see that lattice cutoff effects are suppressed at large flow times but at small flow times they are noticeable. To see down to what flow time the c_1 is free of lattice cutoff effects, we plot the ratio $c_1/c_1(\beta = 7.793)$ in the right panel. In order to see more clearly how the different lattice spacings differ from each other, we have plotted error bars based only on the statistical errors in the coarser lattices—that is, statistical errors in the $\beta = 7.793$ lattice are treated as a common systematic error in the right plot. The figure shows that the lattices give compatible c_1 values as long as the flow time is

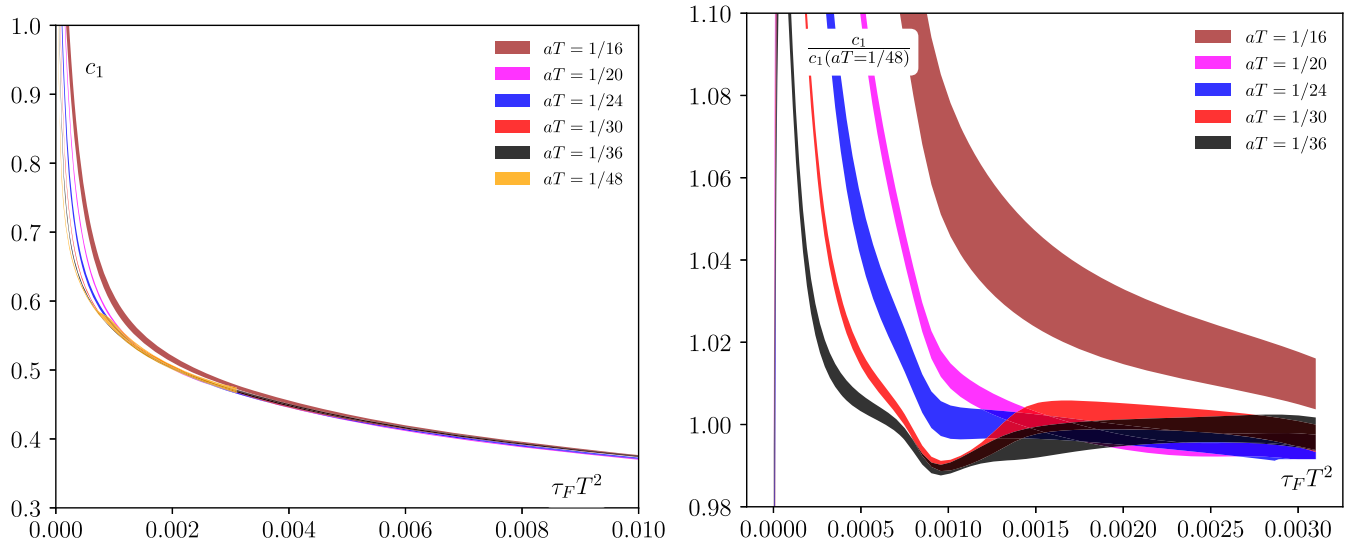

FIG. 2. Left: combined c_1 at different lattice spacings. Right: the ratio of $c_1/c_1(\beta = 7.793)$. The error in the estimation of $c_1(\beta = 7.793)$ is not included in the ratio. because $c_1(\beta = 7.793)$ is only used as a normalization and its error is irrelevant to the rest analysis. The temperature T in the legends aT and $\tau_F T^2$ has been fixed to $1.5T_c$.

large enough, but each lattice starts to deviate at a flow time such that τ_F/a^2 becomes order one. Specifically, in every case the deviation from continuum behavior reaches 2% when $\tau_F \simeq 0.4a^2$. The deviation rapidly becomes more severe below this point. This deviation from continuum behavior indicates that the applied gradient flow is not sufficient to supply a continuumlike, well-renormalized stress-tensor operator. Since the statistical precision of our EMT correlator data is typically around 2% and since we want to keep systematic effects smaller than this, we will impose the condition $\tau_F \geq 0.4a^2$ when we perform the double extrapolation of shear correlators in the next section.

Now we calculate c_2. According to Eq. (11), the running coupling in the $\overline{\text{MS}}$ scheme is needed. For that we first calculate the coupling in the gradient flow-scheme and then convert it to the $\overline{\text{MS}}$ scheme. In the gradient-flow scheme the running coupling can be calculated as [40,41]

$$g^2_{\text{flow}} = \frac{128\pi^2}{3(N_c^2-1)} \frac{1}{1+\delta(\tau_F)} \langle \tau_F^2 E \rangle, \tag{14}$$

where $N_c = 3$ and E is the energy density defined in Eq. (8). $\delta(\tau_F)$ can be found in [40,41] as well. Note that the energy density should be measured at zero temperature. On the lattice we take large temporal extents to suppress the thermal effects. The lattices used to study this quantity are given in Table III. Because of high computation costs the two finest lattices have smaller-aspect ratios. However, based on the three coarse lattices, we have seen that finite volume effects are small compared to the statistical error of the correlators.

After obtaining $\tau_F^2 E$ in the gradient flow scheme, we can relate it to the one in the $\overline{\text{MS}}$ scheme [29]. This requires solving a cubic equation, whose solution gives the running coupling in the $\overline{\text{MS}}$ scheme. Inserting in Eq. (11), we get the final c_2 shown in Fig. 3. The errors are not visible as they are tiny and in every case much smaller than 1%. We can see that

TABLE II. The lattices with smaller temporal extents for the determination of c_1.

β	a[fm](a^{-1}[GeV])	N_τ^h	N_σ^h	#Configuration
6.8736	0.0262 (7.534)	12	64	1000
7.0350	0.0215 (9.187)	10	80	1000
		14	80	1000
7.1920	0.0178 (11.11)	12	96	1000
		18	96	1000
7.3940	0.0140 (14.14)	10	120	1000
		16	120	1000
7.5440	0.0117 (16.88)	12	140	1000
		18	120	1000
		24	120	1000
7.7930	0.0087 (22.78)	12	144	500
		24	144	500
		48	192	700

TABLE III. The lattices at $T < T_c$ for the study of c_2.

a (fm)	a^{-1} (GeV)	N_σ	N_τ	β	T/T_c	#Configuration
0.0262	7.534	64	64	6.8736	0.3776	1000
0.0215	9.187	80	80	7.0350	0.3684	1000
0.0178	11.11	96	96	7.1920	0.3712	1000
0.0140	14.14	96	120	7.3940	0.3780	1000
0.0117	16.88	96	144	7.5440	0.3761	1000

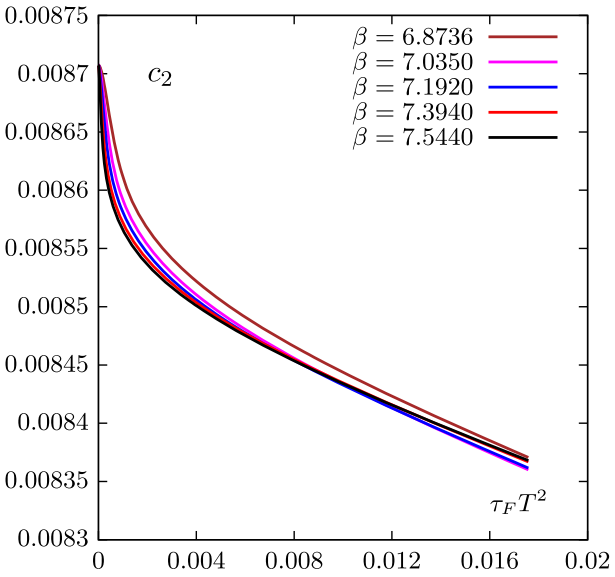

FIG. 3. c_2 measured at $T < T_c$ at different lattice spacings.

unlike c_1, the difference of c_2 among different lattice spacings is always small. The ratio $c_2/c_2(\beta = 7.544)$ is always smaller than 1% at all flow times, suggesting that the cutoff effects can be ignored for c_2.

V. LARGE SEPARATIONS AND NOISE REDUCTION

Evaluating Eq. (6) involves computing a correlator with an integral over all values of the spatial separation. To improve signal-to-noise ratio, in practice one evaluates $\int \mathrm{d}^3x\mathrm{d}^3y\mathrm{d}t\langle T(x,\tau+t)T(y,t)\rangle$, that is, one performs an integral over the coordinates of each operator. The correlation function is dominated by small values of coordinate difference $|x-y|$. However, the fluctuations in the correlator, and therefore the noise, are approximately separation independent. Therefore, the inclusion of large separations makes the evaluation noisy without contributing meaningfully to the signal.

In Ref. [24] we proposed a way to reduce these noise contributions. The operator of interest ($T_{\mu\mu}$ or a component of π_{ij}) is first summed over small volumes called blocks, on a single τ sheet but with a cubic space extent given in Table I. We evaluate all block-to-block correlators and then average all correlators which have the same temporal and block-center spatial separation. Finally, we examine how the correlation function varies with the space separation between blocks, replacing the large-separation, small-signal values with an asymptotic fit as described in [24].

Each index combination of the $\langle \pi_{ij}(x,\tau)\pi_{ij}(y,0)\rangle$ correlator has a distinctive angular structure as a function of the direction of the $\vec{x}-\vec{y}$ vector. For instance, from reflection positivity we know that $\langle T_{xy}(\vec{r})T_{xy}(0)\rangle < 0$ for $\vec{r}$ pointing along the x-axis or y-axis, but it is positive if $\vec{r}$ points along the z-axis or the line $x = y$. In contrast, the $\langle (T_{xx}-T_{yy})(\vec{r})(T_{xx}-T_{yy})(0)\rangle$ correlator is positive along each lattice axis but is negative along the $x = y$ line. In our blocking procedure, certain block separations primarily sample blocks which are separated along lattice axes, while others sample the directions along lattice diagonals or other combinations. Therefore, $T_{xy}T_{xy}$-type correlators will be larger for some blocks and smaller for others, while $T_{xx}-T_{yy}$-type correlators will show the opposite trend. Including a single component or a subset of possible components leads to a correlation function which varies strongly with separation-direction and therefore jumps up and down as a function of the block separation. This effect goes away if we include all traceless ij combinations, which is therefore obligatory. We illustrate this in Fig. 4, which shows the $\pi\pi$ correlation function as a function of block separation.

In general, the lattice renormalization constant c_1 is different for $T_{xx}-T_{yy}$ than for T_{xy}, because the rotational symmetry which relates them in the continuum is absent on the lattice [30,42,43]. We have only evaluated the renormalization constant for the former operator type. However, the application of gradient flow should remove rotation-invariance violations in operator normalizations up to corrections suppressed by $\mathcal{O}(a^2/\tau_{\mathrm{F}})$. Therefore, any effects from this operator normalization issue should be removed in our fixed-τ_{F} continuum limit. A recent masters

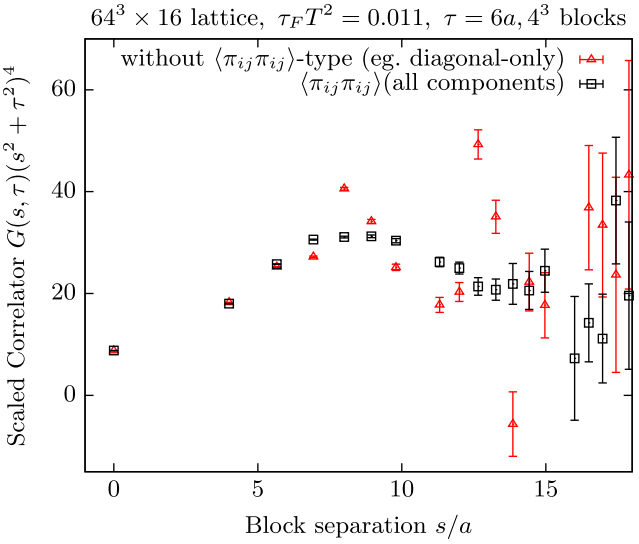

FIG. 4. Traceless spatial stress tensor (shear-channel) correlator between lattice blocks, at a fixed temporal separation, as a function of box separation, together with statistical error bars. The black points contain all traceless stress tensor components, while the red data points contain only the diagonal-type contributions. Some block separations only occur along lattice axes where the diagonal-type contributions are largest, while other block separations occur along lattice diagonals where some diagonal-type contributions are negative. Hence, the red points jump around, while the black points follow a smooth curve until the statistical errors become large.

thesis[1] explores both renormalization constants as a function of flow and finds that they are consistent with each other within 2% error bars already for $\tau_F/a^2 = 0.4$, the smallest value used here.

In order to remove the large-separation data and therefore its noise, it is necessary to fit the large-separation tail to a physically-motivated Ansatz. The fitted value is then used instead of the data at those separations where the block-by-block signal-to-noise ratio is poor. For our Ansatz we will use the leading-order perturbative behavior of the correlation function, accounting for time periodicity, gradient flow, and our blocking procedure. In vacuum, the leading-order correlator of two field strength tensors is

$$\langle F^a_{\mu\nu}(r)F^b_{\alpha\beta}(0)\rangle = \frac{g^2\delta_{ab}}{\pi^2 r^4}\left[\delta_{\mu\alpha}\delta_{\nu\beta} - \delta_{\mu\beta}\delta_{\nu\alpha} - \frac{2}{r^2}(r_\mu r_\alpha\delta_{\nu\beta} - r_\mu r_\beta\delta_{\nu\alpha} - r_\nu r_\alpha\delta_{\mu\beta} + r_\nu r_\beta\delta_{\mu\alpha})\right]. \tag{15}$$

Applying gradient flow to a depth τ_F modifies this expression to [39]

$$\langle G^a_{\mu\nu}(r)G^b_{\alpha\beta}(0)\rangle_{\tau_F} = \frac{g^2\delta_{ab}}{\pi^2 r^4}\left[A(r,\tau_F)(\delta_{\mu\alpha}\delta_{\nu\beta} - \delta_{\mu\beta}\delta_{\nu\alpha}) + \frac{B(r,\tau_F)}{r^2}(r_\mu r_\alpha\delta_{\nu\beta} - r_\mu r_\beta\delta_{\nu\alpha} - r_\nu r_\alpha\delta_{\mu\beta} + r_\nu r_\beta\delta_{\mu\alpha})\right], \tag{16}$$

$$A(r,\tau_F) = 1 - \left(1 + \frac{r^2}{8\tau_F}\right)e^{-r^2/8\tau_F}, \qquad B(r,\tau_F) = -2 + \left[2 - 2\frac{r^2}{8\tau_F} + \left(\frac{r^2}{8\tau_F}\right)^2\right]e^{-r^2/8\tau_F}. \tag{17}$$

Note that this is a continuum, not lattice, expression; but when $\tau_F/a^2 > 0.5$, the lattice-continuum difference for flowed correlators is small, and the use of a continuum limit at fixed flow depth based only on data which satisfies this criterion should avoid the need to include lattice spacing corrections as well.

Using these expressions, at finite $\tau_F, \tau, |\vec{r}|$ and with periodic boundaries in the time direction, the leading-order stress tensor correlator summed over all transverse-traceless elements $\hat{T}_{ij} = T_{ij} - \delta_{ij}T_{kk}/3$ relevant for shear viscosity and for bulk viscosity are

$$\langle \hat{T}_{ij}(\vec{r},\tau)\hat{T}_{ij}(0,0)\rangle_{\tau_F} \propto \sum_{n_1,n_2\in\mathcal{Z}} \frac{A(r_1)A(r_2)}{r_1^4 r_2^4} + \frac{A(r_1)B(r_2) + A(r_2)B(r_1)}{2r_1^4 r_2^4} + \frac{B(r_1)B(r_2)}{6r_1^6 r_2^6}\left(3(r_1\cdot r_2)^2 + \vec{r}^2\left[r_1^2 + r_2^2 - 4r_1\cdot r_2 + \frac{4}{5}\vec{r}^2\right]\right), \tag{18}$$

$$\langle T_{\mu\mu}(\vec{r},\tau)T_{\nu\nu}(0,0)\rangle_{\tau_F} \propto \sum_{n_1,n_2\in\mathcal{Z}} \frac{A(r_1)A(r_2)}{r_1^4 r_2^4} + \frac{A(r_1)B(r_2) + A(r_2)B(r_1)}{2r_1^4 r_2^4} + \frac{B(r_1)B(r_2)}{6r_1^6 r_2^6}(2(r_1\cdot r_2)^2 + r_1^2 r_2^2), \tag{19}$$

where $r_1 = (\tau + n_1\beta, \vec{r})$ and $r_2 = (\tau + n_2\beta, \vec{r})$ are the 4-displacement with the temporal displacement shifted by independent integer multiples of the inverse temperature β.

VI. TEMPERATURE CORRECTION AND TREE LEVEL IMPROVEMENT

From Table I it can be seen that the temperatures are not exactly $1.5T_c$ on all lattices. This setup is adopted for historical reasons [44,45], and the deviations of the temperature were only discovered after the correlators were measured. The temperature differences, though small, must be accounted for when performing a continuum extrapolation. Because the temperature differences are small and the lattices are fine enough that the continuum extrapolation is not very severe, we will content ourselves by evaluating the temperature dependence at the linearized level and at a single lattice spacing. We then assume that the established temperature correction also applies at the other lattice spacings. We choose to perform a linear temperature-dependence analysis on the lattice which has the largest deviation from $T = 1.5T_c$, namely the 20×80^3 lattice with $\beta \equiv \beta_1 = 7.035$ and $T = 1.4734T_c$. For this lattice, we choose a second β value, $\beta_2 = 7.0767$, corresponding to $T = 1.5501T_c$, and we repeat our correlation function studies on this lattice. Since the renormalized correlators

[1]Jonas Winter, private communication.

contain two parts, namely the renormalization constants c_1 or c_2 and the bare correlators, the corrections for both parts should be considered. The renormalization constants have been determined precisely in Sec. IV at β values listed in Table I. To obtain the one at $\beta = 7.0767$ we linearly interpolate between $\beta = 7.035$ and $\beta = 7.192$. We then calculate the renormalized correlators, denoted as G_1 and G_2 for the lower and higher temperature, respectively, by multiplying the bare correlations functions and the squared renormalization constants. We then evaluate the difference, $-1 + G_2(\tau)/G_1(\tau)$, representing the temperature dependence of the correlation function, as a function of τ and τ_F. Statistical errors are computed using bootstrap sampling, and since G_1, G_2 arise from different ensembles, their errors are independent and can be propagated via Gaussian error propagation.

Figure 5 shows the thermal correction for the largest gradient flow depth we use (and therefore the least noisy data). The figure shows that the temperature effect is nearly τ independent except at the smallest τ values (which are contaminated by lattice effects). Based on this result, we treat $-1 + G_2/G_1$ as a function of τ_F only, determining its value based on the weighted average of all the points at $\tau/a \geq 4$ at each τ_F. As the figure shows, the thermal corrections are relatively small, considering that the temperature difference $1.5501 - 1.4734 = 0.0767T_c$ is significantly larger than any of the individual deviations from $1.5T_c$ shown in Table I. We will therefore use the determined slope $P = (G_2/G_1 - 1)/(T_2 - T_1)$, averaged over τ values, and apply it as a linearly interpolated correction to all data. For instance, data at temperature T can be interpolated to the temperature T_0 through $G(T_0) \simeq G(T)(1 + P(T_0 - T))$. A detailed analysis on the uncertainties in the temperature correction can be found in Appendix B. The appendix also presents an alternative model, which gives a consistent result.

Next, consider discretization effects associated with computing on a lattice rather than in continuous space. To suppress the lattice discretization effects, we apply tree level improvement to the bare correlators. Specifically, if we assume that the lattice correlation functions will deviate from the continuum ones in the same way as occurs at lowest-perturbative order, then we can remove this effect by rescaling by the ratio of leading-order continuum to lattice-correlation functions [46,47],

$$G^{\text{t.l.}}(\tau T) = G_{\text{lat}}(\tau T) \cdot \frac{G^{\text{LO}}_{\text{cont}}(\tau T)}{G^{\text{LO}}_{\text{lat}}(\tau T)}. \tag{20}$$

The leading-order continuum correlators in shear channel and bulk channel can be found in [13,14]

$$\begin{aligned} \frac{G^{\text{LO,shear}}_{\text{cont}}(\tau T)}{T^5} &= \frac{32 d_A}{5\pi^2}\left(f(x) - \frac{\pi^4}{72}\right), \\ \frac{G^{\text{LO,bulk}}_{\text{cont}}(\tau T)}{T^5} &= \frac{484 d_A}{16\pi^6} g^4 \left(f(x) - \frac{\pi^4}{60}\right), \end{aligned} \tag{21}$$

where $x = 1\text{–}2\tau T$, $f(x) = \int_0^\infty ds\, s^4 \cosh^2(xs)/\sinh^2 s$ and $d_A = 8$ counting the number of gluons. The leading-order lattice correlator for clover discretization is available in [47]. For better visibility we always normalize the tree-level improved correlators with a normalization correlator G_{norm} calculated at $\tau_F = 0$, where for shear channel we use $G_{\text{norm}} \equiv G^{\text{LO,shear}}_{\text{cont}}$ and for bulk we use $G_{\text{norm}} \equiv G^{\text{LO,bulk}}_{\text{cont}}/g^4$.

After temperature corrections, tree-level improvement and renormalization, in Fig. 6 we show the lattice

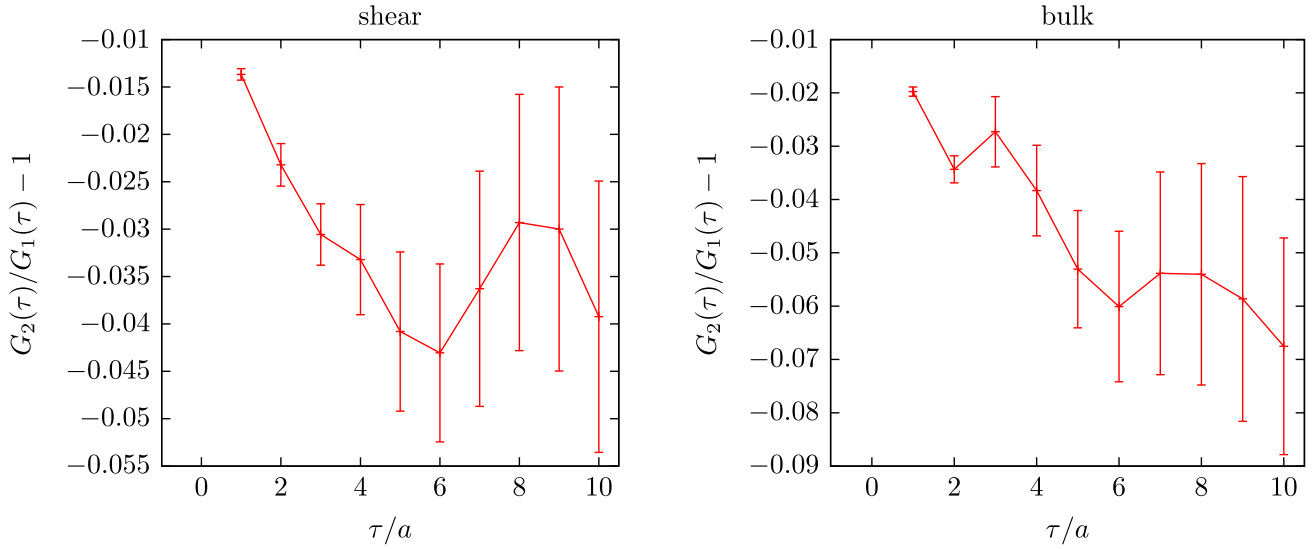

FIG. 5. The temperature correction when going from $\beta_1 = 7.035$ to $\beta_2 = 7.0767$ on an $80^3 \times 20$ lattice, for shear (left) and bulk (right). Each data point is found at the maximum flow time used in the flow-time extrapolation (see Sec. VII).

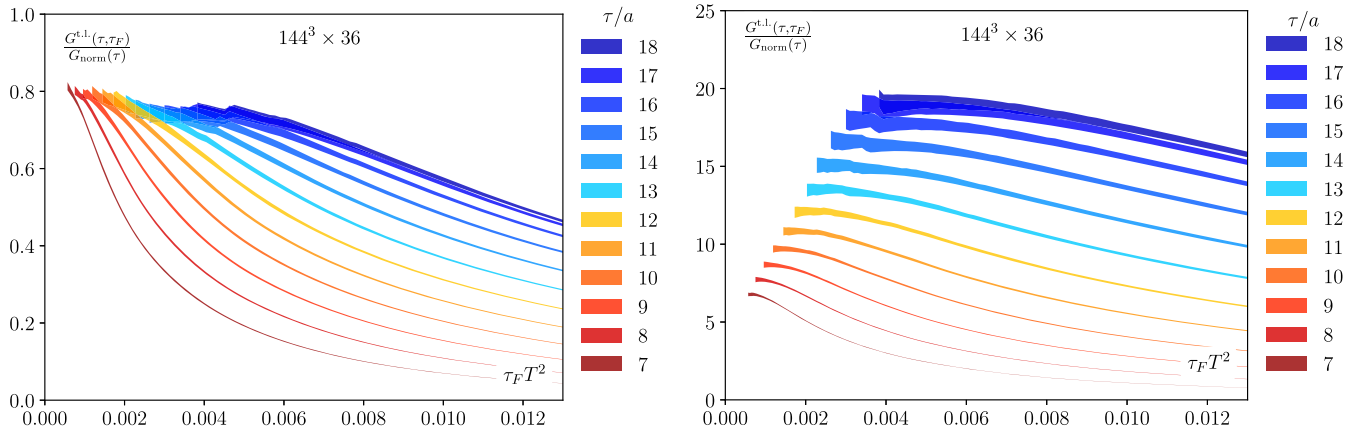

FIG. 6. Tree-level-improved EMT correlators in the shear channel (left) and bulk channel (right) normalized by the leading-order correlator on the $144^3 \times 36$ lattice at different flow times. (The tree-level correlator used for the normalization in the bulk channel is missing a factor of g^4, which explains the large ratio.)

correlators normalized by the free continuum correlators on $144^3 \times 36$ lattice at different flow times, in both the shear and the bulk channels. We have not plotted data down to small flow times because it has large errors. We can see that as flow time increases the signal-to-noise ratio improves. At very large flow times the signal is strongly modified by flow effects and we leave the regime where an extrapolation $\tau_{\text{F}} \to 0$ can be performed.

VII. DOUBLE EXTRAPOLATION

The double extrapolation contains two steps: first we perform the continuum extrapolation $a \to 0$, and then we perform a flow-time-to-zero extrapolation. As we pointed out in Ref. [18], this has the advantage that the continuum extrapolation eliminates terms of form a^2/τ_{F}, so that the τ_{F} extrapolation will consist only of positive powers. Before the continuum extrapolation, the correlators on coarse lattices have to be interpolated to the separations of the finest lattice, for details see, for example, references [18,48]. In the continuum extrapolation we use the Ansatz

$$\frac{G^{\text{t.l.}}(N_\tau)}{G_{\text{norm}}(N_\tau)} = m \cdot N_\tau^{-2} + b, \tag{22}$$

because the lattice action has leading discretization errors of order a^2. Here m and b are fit parameters that can be different for each temporal separation and flow time. The continuum estimates for the (normalized) correlators are given by $b \equiv G_{\text{cont}}/G_{\text{norm}}$.

Figure 7 shows how good the fit Ansatz, Eq. (22), works at an intermediate flow time $\tau_{\text{F}}T^2 = 0.00416$. We can see for the bulk channel that in some cases the fit is poor in the sense that $\chi^2/\text{dof} > 1$. Our procedure is to enlarge the error bars by $\sqrt{\chi^2/\text{dof}}$ in these cases. After the continuum extrapolation we collect the continuum estimates for each flow time and show them in gray bands in Fig. 8.

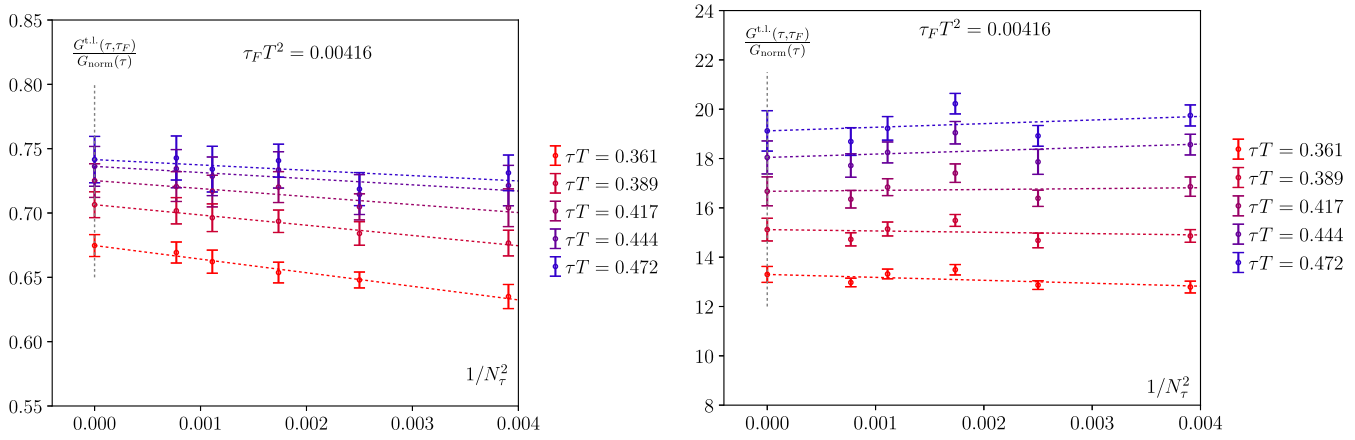

FIG. 7. The continuum extrapolation of EMT correlators in shear channel (*left*) and bulk channel (*right*) at flow time $\tau_{\text{F}}T^2 = 0.00416$, fit using Eq. (22). The error bars on data points are statistical; the errors on the extrapolated values are the uncertainties from the extrapolated fit.

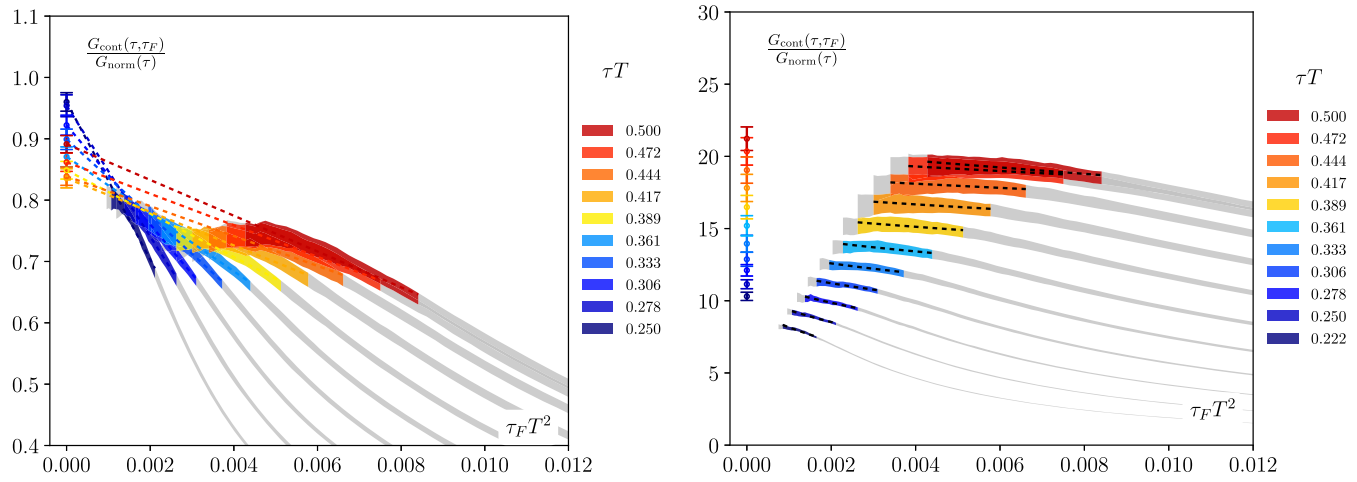

FIG. 8. The $\tau_{\rm F} \to 0$ extrapolation of continuum-extrapolated EMT correlators in the shear channel (*left*) and bulk channel (*right*).

Now we consider the $\tau_{\rm F} \to 0$ extrapolation. To perform the extrapolation, we need to understand the functional dependence on $\tau_{\rm F}$, and we need to determine over what range of $\tau_{\rm F}$ values to perform the extrapolation. For general values of $\tau_{\rm F}/\tau^2$, the correlator is a complicated function of this ratio, in some cases even taking on a different sign than the small-$\tau_{\rm F}$ value [39]. However, if $\tau_{\rm F}/\tau^2$ is small, then as discussed near the end of Sec. II, we expect the flowed stress tensor to be described in terms of an operator product expansion, with the leading coefficient equaling the stress tensor and with higher-dimension operators suppressed by powers of $\tau_{\rm F}$. As a result, in this regime the small-$\tau_{\rm F}$ expansion of the correlation function should approach $\tau_{\rm F} \to 0$ with polynomial-in-$\tau_{\rm F}$ corrections. (We will ignore possible anomalous dimensions in this discussion.)

The more fitting coefficients we use, the larger the errors in the resulting fit. Therefore, we want to avoid using two extrapolation coefficients, e.g., a fit of form $G(\tau_{\rm F}/\tau^2) = A + B\tau_{\rm F}/\tau^2 + C\tau_{\rm F}^2/\tau^4$. And if we use a wide enough data range that the $\tau_{\rm F}^2/\tau^4$ coefficient is really relevant, then there is a danger that we also need still higher-order coefficients. Therefore, we will restrict ourselves to a region where the total variation in $G(\tau_{\rm F}/\tau^2)$ appears to be at most 20% from its extrapolated value. In this range, within the few % accuracy which is our goal, we expect that a linear extrapolation, e.g., $G(\tau_{\rm F}/\tau^2) = A + B\tau_{\rm F}/\tau^2$, should be sufficient. Based on our previous experience with the topological density operator [48], we expect that a fitting range out to $\sqrt{8\tau_{\rm F}^{\rm max}} = 0.5220\tau$ should remain in this small-correction regime. We will fit a range of $\tau_{\rm F}$ from this maximum down to half this value, because the correlator becomes so noisy at smaller $\tau_{\rm F}$ that extending the range further is not helpful. In addition, to prevent lattice spacing effects of form $a^2/\tau_{\rm F}$, we restrict to values with $\tau_{\rm F}/a^2 \geq 0.4$ as already discussed. For small τ values this constraint excludes too much of the $\tau_{\rm F}$ range over which we want to extrapolate, which prevents us from determining the correlator at small temporal separations. The resulting correlators within the range $[0.5\tau_{\rm F}^{\rm max}, \tau_{\rm F}^{\rm max}]$ are shown as colored bands in Fig. 8.

For the extrapolation of the bulk viscosity correlators we have taken a slightly different approach, based on the work of [25,26,49]. A recent three-loop calculation of the flow-dependence of the EMT trace suggests a finite-$\tau_{\rm F}$ fitting function of form [26]

$$\theta(\tau_{\rm F}) = \left(1 - c\left(\frac{g^2(\mu(\tau_{\rm F}))}{(4\pi)}\right)^3\right)\theta(\tau_{\rm F} = 0), \qquad (23)$$

where c and $\theta(\tau_{\rm F} = 0)$ are fit parameters. Since what we measured in this study is the correlators of θ, we take the square root of the correlators and fit it to Eq. (23). The fitted curves are shown as dashed black lines in Fig. 8 and the extrapolated correlators are shown as colored points at $\tau_{\rm F}T^2 = 0$. It can be seen that the fit function is almost linear, indicating that a fit to an Ansatz linear in flow time (as used in [18,48]) would give similar results. Appendix C presents more details on both the continuum and the small flow-time extrapolations. The double extrapolated correlators in both channels are shown in Fig. 9.

VIII. SPECTRAL ANALYSIS

This section is devoted to the spectral extraction from the extrapolated correlators. We first reconstruct the spectral function using χ^2-fits with models based on perturbative calculations and then determine the viscosities using the Backus-Gilbert (BG) method [50].

The spectral reconstruction performed here is mathematically ill-posed [51]. One feature of this is the difficulty in quoting a robust spectral function since uniqueness of any solution is *a priori* not given.

In the case of the spectral analysis via fit this issue presents itself as the difficulty in finding a global, well-determined minimum. In principle, if the "correct" Ansatz were known,

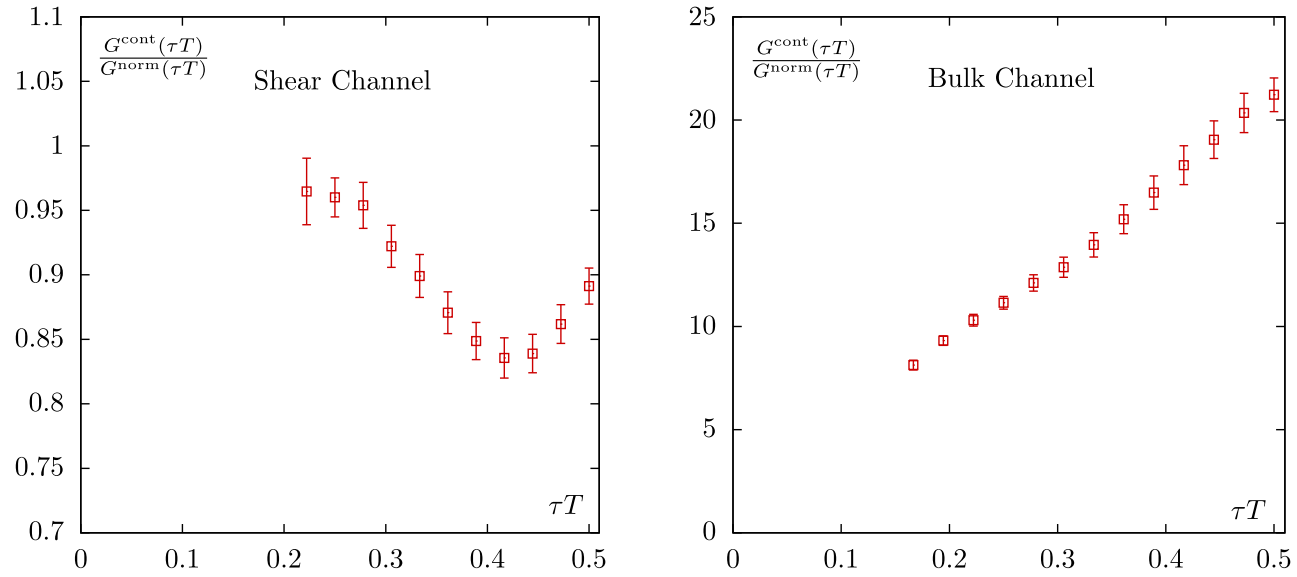

FIG. 9. Double-extrapolated correlators in the shear channel (*left*) and bulk channel (*right*). Note that $G^{\rm norm}(\tau T)$ in the bulk channel is missing a factor of g^4, which explains the size and possibly the slope of the resulting correlator ratio.

with enough data points and without considering any noise the analysis should yield a global minimum in the χ^2-plane. Without this knowledge and with noise included, however, this minimum is less well determinable and a fit often yields χ^2-values that are not very sensitive to the parameter choices. Consequently, it becomes difficult to choose with confidence which solution and Ansatz is the best description. In the following we address this difficulty by augmenting our study with a spectral analysis using a method that does not rely on an Ansatz *per se* in form of the BG method.

A. Spectral function from model fits

According to Eqs. (1) and (3), the viscosities are proportional to the slope of the spectral function at zero frequency. But the large frequency part also contributes considerably to the correlators and they can be computed perturbatively. For the shear channel the large frequency part has been computed both at leading order (LO) and at next-to-leading order (NLO) [52],

$$\rho^{\rm LO}_{\rm shear}(\omega) = \frac{d_A\omega^4}{10\pi}\coth\left(\frac{\omega}{4T}\right),$$
$$\rho^{\rm NLO}_{\rm shear}(\omega) = \rho^{\rm LO}_{\rm shear}(\omega) - 4d_A\omega^4\coth\left(\frac{\omega}{4T}\right)\frac{g^2(\bar\mu)N_c}{(4\pi)^3} \times\left[\frac{2}{9}+\phi^\eta_T(\omega)\right]. \tag{24}$$

Note that our definition of the spectral function differs from that in Ref. [52] by a relative minus sign. Here $d_A = N_c^2-1=8$ is the dimension of the adjoint representation. In the region of $\omega \ll \pi T$, the one-loop running coupling can be fixed via the "EQCD" renormalization point [53]

$$\ln(\bar\mu^{{\rm opt}(T)}) \equiv \ln(4\pi T) - \gamma_{\rm E} - \frac{1}{22}. \tag{25}$$

Using this relation the coupling is fixed to the value $g^2(\bar\mu^{{\rm opt}(T)}) = 2.2346$ at $T = 1.5T_c$, where we use an updated relation $T_c = 1.24\Lambda_{\overline{\rm MS}}$ [34]. For large ω, due to the lack of explicit logarithms of the renormalization scale in Eq. (24), a natural choice is given by $\bar\mu^{{\rm opt}(\omega)} = \omega$ [52]. Combining the above two conditions a switching point for the renormalization scale at $\omega/T = 2.146\pi$ can be found. The dimensionless function $\phi^\eta_T(\omega)$ was first determined in Ref. [52] but with a computational error, which was found in Ref. [54]. In [54] another term from HTL resummation was introduced. Such a term only affects small frequencies and we do not include it in our spectral analysis, as we do not expect HTL to be reliable at the nonperturbative regime of small frequencies.

For the bulk channel the LO and NLO spectral function are also available [55]

$$\rho^{\rm LO}_{\rm bulk}(\omega) = \frac{d_A c_\theta^2\omega^4 g^4}{4\pi}\coth\left(\frac{\omega}{4T}\right),$$
$$\rho^{\rm NLO}_{\rm bulk}(\omega) = \rho^{\rm LO}_{\rm bulk}(\omega) + d_A c_\theta^2\omega^4\coth\left(\frac{\omega}{4T}\right)\frac{g^6(\bar\mu)N_c}{(4\pi)^3} \times\left[\frac{22}{3}\ln\frac{\bar\mu^2}{\omega^2}+\frac{73}{3}+8\phi_T(\omega)\right], \tag{26}$$

where $c_\theta \approx -b_0/2 - b_1 g^2/4$, $b_0 = \frac{11N_c}{3(4\pi)^2}$ and $b_1 = \frac{34N_c^2}{3(4\pi)^4}$. $\phi_T(\omega)$ can be found in [55]. At LO, the running coupling can not be fixed. For simplicity we fix it to the one at the switching point at NLO. One can also fix it to another point, however this will not have effect on our spectral reconstruction as we shall see later there will be a rescaling factor to account for this uncertainty. At NLO, for $\omega \gg \pi T$

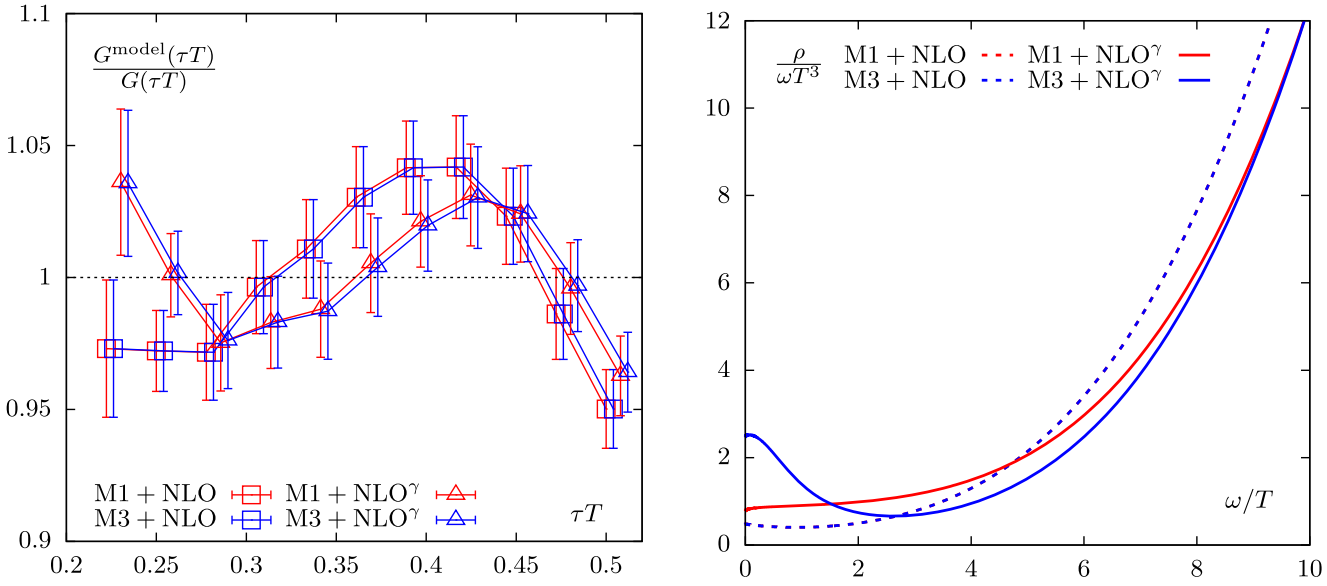

FIG. 10. The comparison of fit correlators and lattice correlators (left) and the fit spectral function in the shear channel. In M3 the width of the Lorentzian peak C has been fixed to 1.

the optimization of the scale $\bar{\mu}$ and the running coupling can be determined [55]

$$\ln(\bar{\mu}^{\text{opt}(\omega)}) \equiv \ln(\omega) - \frac{73}{44}. \tag{27}$$

In the opposite regime one should use Eq. (25). Equating Eqs. (25) to (27) leads to a switching point $\omega/T = 11.276\pi$. For an arbitrary ω the larger optimization scale from the two equations should be used.

The infrared behavior of the spectral function is not known *a priori*, and must be modeled. In previous work [48] we have considered several proposed IR behaviors, generally finding that the data is not very restrictive between different IR Ansätze choices. In this work we will consider one model with an infrared "peak" and perturbative UV behavior, and two "peak-free" models in which the IR behavior is linear in ω, the UV behavior is perturbative, and the spectral function increases continuously between them,

$$\begin{aligned}
\text{M1}: \ & \frac{\rho(\omega)}{\omega T^3} = \frac{A}{T^3} + B\frac{\rho_{\text{pert}}(\omega)}{\omega T^3}, \\
\text{M2}: \ & \frac{\rho(\omega)}{\omega T^3} = \sqrt{\left(\frac{A}{T^3}\right)^2 + \left(B\frac{\rho_{\text{pert}}(\omega)}{\omega T^3}\right)^2}, \\
\text{M3}: \ & \frac{\rho(\omega)}{\omega T^3} = \frac{A}{T^3}\frac{C^2}{C^2 + (\omega/T)^2} + B\frac{\rho_{\text{pert}}(\omega)}{\omega T^3}.
\end{aligned} \tag{28}$$

Here B is a coefficient allowing for a rescaling of the perturbative result, and A is the size of the IR contribution, which determines the transport coefficient of interest. In the first model, we consider a simple sum of an IR and a UV behavior; in the second, we consider a smooth switch-over between IR and UV behavior. In the third model, the IR behavior is a Lorentzian with width parameter C. For simplicity, we have fixed the width parameter C to unity, but we also explored other values and we find a rather weak dependence of the fit quality on the choice. We will use the range of fit values for A between these models as an estimate of the value and uncertainty in the viscosity, though realistically the true spectral function may look different than any of our models and this introduces a potentially large systematic uncertainty in our final result. In addition, for the bulk-viscous channel, there is a known constant contribution arising from the dependence of $T_{\mu\mu}$ on the energy density and on the fluctuations in the system energy. Specifically, the spectral function is known to possess a delta function at zero frequency, equal to $\rho/\omega T^3 = \pi\frac{E+P}{T^3}\frac{(3c_s^2-1)^2}{c_s^2}\delta(\frac{\omega}{T})$. Equivalently, one can subtract an τ-independent constant of corresponding size from the Euclidean correlation function. We adopt the values $\frac{E+P}{T^3} = 5.098$ and $c_s^2 = 0.2848$ that can be calculated from [38].

For the bulk channel our fit has two parameters on 13 data points, leaving 11 degrees of freedom. The leading-order fit shows a poor χ^2/dof, with values of 3.9, 5.4 and 6.3 for M1, M2, and M3 with $C = 1$. But using the NLO spectral function returns a good fit, with χ^2/dof of 0.4, 0.5 and 0.6. This suggests that the NLO corrections and in particular the running of the coupling improve the estimation significantly and brings it close to our nonperturbative determination. The resultant ζ/T^3 is 0.086(0.008), 0.133 (0.010), and 0.303(31) for M1, M2, and M3($C = 1$), respectively.

For the shear channel we find that when using the LO spectral function the χ^2/dof is 4.1, 3.99, and 3.98, and for

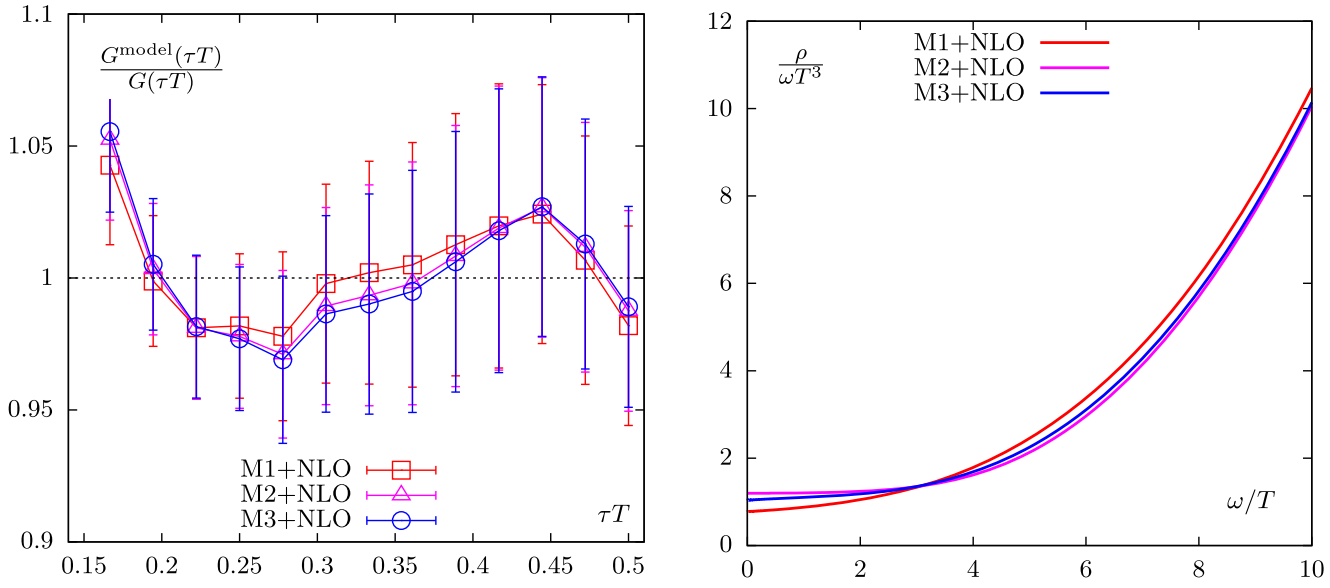

FIG. 11. The comparison of fit correlators and lattice correlators (left) and the fit spectral function in the bulk channel.

the NLO spectral function it is 3.7, 4.8, and 3.66, respectively. This indicates that both LO and NLO calculations fail to capture our nonperturbative results for the Euclidean correlator. This indicates that the true form of the spectral function is something more complicated than our relatively simple proposals in Eq. (28).

As one attempts to capture possibly missing structure, we have considered amending the UV part of the spectral function with an anomalous dimension, namely changing Eq. (24) by replacing ω^4 with $\omega^{4+\gamma}$. With this modification we find that the χ^2/dof becomes $\sim 2.0-2.1$ for all models, both for the LO and the NLO spectral function. The returned value of the viscosity, with statistical errors, is $\eta/T^3 = 0.84(0.14)$, 1.10(0.14) for LO and 0.77(0.16) and 1.09(0.15) for NLO, all using the first two models. Model M3 with $C = 1$ using NLO and an anomalous dimension returns $\eta/T^3 = 2.46(54)$. Using an anomalous dimension improves the fit, but χ^2/dof of 2 with eight degrees of freedom still represents a rather poor fit. We show the ratio of fit correlators to the lattice data, and the resulting spectral functions in Figs. 10 and 11 for the shear and bulk channel, respectively. It would be interesting to explore other models for the IR behavior and to see if any such model can improve the quality of our fit.

B. Spectral function from Backus-Gilbert method

The technical difficulty in performing the spectral reconstruction can be traced in part to two issues, the finiteness of the number of data points and their noise. The first implies a discretization of the integral transform

$$G(\tau) = \int_0^\infty \mathrm{d}\omega \rho(\omega) K(\tau,\omega) \rightsquigarrow G(\tau_i) = \sum_{i=1}^{N_\tau} \rho(\omega)\tilde{K}(\tau_i,\omega) \tag{29}$$

i.e., the underlying task is an inverse problem to find ρ at a given ω, schematically written as $\rho = \sum_i \tilde{K}_i^{-1} G_i$.

Consider an estimator $\hat{\rho}$ of the spectral function at a given $\bar{\omega}$ by (see e.g., [56,57])

$$\hat{\rho}(\bar{\omega}) = f(\bar{\omega}) \int_0^\infty \mathrm{d}\omega\, \delta(\bar{\omega},\omega)\rho(\omega) f(\omega)^{-1}, \tag{30}$$

where $f(\omega)$ is an arbitrary rescaling function and $\delta(\bar{\omega},\omega)$ is a smooth function, normalized to $\int_0^\infty d\omega\delta(\bar{\omega},\omega) = 1$, that may be parametrized as $\delta(\bar{\omega},\omega) = \sum_i q_i(\bar{\omega})K(\tau_i,\omega)$ [50]. This so-called resolution function acts as an averaging kernel that enables formulating the spectral function estimator as

$$\hat{\rho}(\bar{\omega}) = f(\bar{\omega})\sum_i q_i(\bar{\omega})G(\tau_i). \tag{31}$$

In this form it becomes clear that constructing $\hat{\rho}$, or by extension ρ, depends crucially on the number of coefficients available, i.e., the number of data points, and their behavior (how stable and regular the inverse is). Typically one is faced with a situation where the coefficients are large and highly fluctuating, requiring very precise determinations, but at the same time the connected matrix is nearly singular, requiring a regulator to be inverted safely. The added effect of noise in the data further complicates this situation as it affects the precision with which the coefficients can be determined.

Keeping this in mind, one recipe to evaluate $\hat{\rho}(\bar{\omega})$ is given by the Backus-Gilbert method (BGM) [50]. Construct the coefficients q_i such that the width Γ, or spread, of the resolution function in ω becomes minimal, i.e., in the ideal case $\lim_{\Gamma\to 0}\hat{\rho} = \rho$. Then the solution can be shown to be

$$q_i(\bar{\omega}) = \frac{\sum_j W_{ij}^{-1}(\bar{\omega})R(\tau_j)}{\sum_{kj} R(\tau_k)W_{kj}^{-1}(\bar{\omega})R(\tau_j)}, \tag{32}$$

$$W_{ij}(\bar{\omega}) = \lambda \int_0^\infty \mathrm{d}\omega K(\tau_i,\omega)(\omega-\bar{\omega})^2 K(\tau_j,\omega) + (1-\lambda)S_{ij},$$
$$R(\tau_i) = \int_0^\infty \mathrm{d}\omega K(\tau_i,\omega). \tag{33}$$

Here we immediately introduced a regularization scheme $W_{ij} = \lambda W_{ij}^{\mathrm{noreg}} + (1-\lambda)S_{ij}$, where S is the covariance matrix of the lattice correlators and $0 \leq \lambda \leq 1$ is the regularization parameter. Other regularization schemes, such as the Tikhonov scheme where $S_{ij} = \mathbb{1}$, have also been used in literature, see e.g., [16]. Another recipe where the $q_i(\bar{\omega})$ are determined with a fixed input resolution function was presented in [58].

In our implementation we further consider the rescaling function $f(\bar{\omega})$ [57]. It rescales the spectral function inside the integral of Eq. (30) prior to reconstruction and is or may be reintroduced afterwards. The coefficients q_i are changed as a result and the procedure can be understood as related to a kernel transformation. In particular divergent behaviors of the kernel, such as that at $\omega \to 0$ can be handled in this way. Additionally certain well established, global trends of the spectral function can be built-in, for example the large frequency behavior $\sim\omega^4$. As such the procedure can also be seen as introducing prior information and some level of model dependence. Here we consider the function $f = (\omega/T)^4/\tanh^3(\omega/4T)$ introduced to regularize the divergence at $\omega = 0$ and to encode the information on the asymptotic trend.

One key difficulty in the BGM, or any spectral reconstruction, is the determination of its errors, both statistical and systematic. The number of points, the rescaling function, the regularization parameter and the noise of the data all feed into the estimator result. Here, we focus on the impact of the regularization parameter λ. We also tested the impact of using different numbers of points and rescaling functions, but find that using the maximum number of points that have a stable solution and the above mentioned scaling function f lead to the smallest spread of the resolution function. So in this study we use all the available data points. Note that λ to some extent also controls the impact of noise given by the covariance through the regularization prescription.

Choosing λ one would like to use the value which minimizes $\Gamma(\delta(\bar{\omega},\omega))$ in the frequency window of interest. In the left panel of Fig. 12 we show the resolution function dependence for a broad range λ in the shear channel. We see that the width is $\Gamma(\delta(\bar{\omega},\omega)) \sim 5T$ except for the two smallest λ, which implies that the dependence of Γ on λ is weak. At the same time, when plotting the obtained spectral functions depending on λ in the right panel of Fig. 12, we see that the variance of the spectral function and crucially the value of the intercept at $\bar{\omega} = 0$ depend strongly on this parameter. Based on the discussion above the increasing variance with λ can be understood as insufficient regularization, while the decreasing variance with λ but increasing width of the resolution implies the data and coefficients cannot be combined to form sharp, localized features.

Nevertheless, a robust result over a broad range in λ implies a stable solution of the reconstruction. As such scanning through λ in (0,1) does suggest a lower bound for

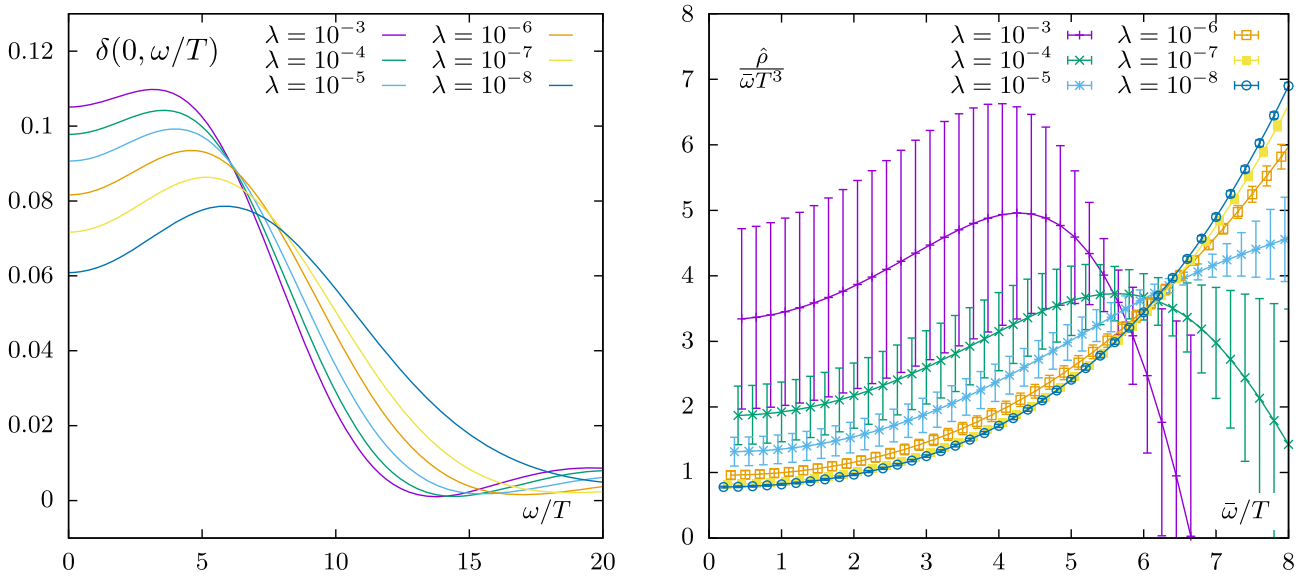

FIG. 12. The resolution function (left) and output spectral function (right) at $\bar{\omega} = 0$ in shear channel at some selected λ values from Backus-Gilbert analysis.

the intercept and thereby the viscosity. For the shear viscosity we find $\eta/T^3 \geq 0.81$ (see right panel of Fig. 12). Similarly for bulk viscosity we obtain $\zeta/T^3 \geq 0.059$. We can see the fit results determined in previous section safely lie in this range.

One could imagine using a criterion for λ based on the variance of the output spectral function instead of the spread of the resolution function, given the strong dependence observed,. The Morozov discrepancy principle [59] could be used for this: It states that $\delta\hat{\rho}(\bar{\omega})/\hat{\rho}(\bar{\omega}) = \overline{\delta G(\tau)}/G(\tau)$, where $\overline{\delta G(\tau)}$ denotes the average correlator variance. Since we are mainly interested in $\bar{\omega} = 0$ one could impose this condition by matching $\delta\hat{\rho}(0)/\hat{\rho}(0) = \delta G(T/2)/G(T/2)$, as the long-$\tau$ correlator data dominates the low-ω spectral function regime [60]. This neglects the resolution function and the matching gives just a rough approximation to the more complicated underlying relation. However, applying this criterion we arrive at results for η/T^3 and ζ/T^3 that agree with the quoted plateau values above.

IX. CONCLUSION

We have calculated the energy-momentum tensor correlators in both the shear and the bulk channel at $1.5T_c$ in the quenched approximation on five large and fine lattices. To improve the signal-to-noise ratio we have applied both the gradient flow method and the blocking method. We thoroughly studied the temperature corrections and the renormalization of the operators. The correlators have been extrapolated first to the continuum limit and then to the $\tau_F \to 0$ limit. The final correlators are used to extract the shear and bulk viscosity based on perturbative models. For the bulk channel, we find that the NLO spectral function can describe our lattice data when adding a transport part with appropriate interpolation. For the shear channel we were unable to find a fit with better than $\chi^2/\text{d.o.f.} = 2$. To further improve the fit quality, we need either a more flexible model or a better theoretical understanding of the expected spectral function.

In fitting our data, we find that the statistical errors are significantly smaller than the difference in fit values found from various-fit Ansätze choices, despite relatively little difference in the fit quality from the different Ansätze choices. This is summarized in Table IV. Therefore we will estimate the lowest and highest value of viscosity to be the extreme values we found among the fit functions. Using $s/T^3 = 5.098$ from [38], our shear and bulk results become

$$\begin{aligned} \eta/s &= 0.15 - 0.48, \qquad T = 1.5T_c, \\ \zeta/s &= 0.017 - 0.059, \qquad T = 1.5T_c. \end{aligned} \tag{34}$$

The lower estimates are above the lower bounds from the Backus-Gilbert analysis. The upper bounds are based on a model which assumes that there *is* a relatively narrow feature near $\omega = 0$, namely a Lorentzian-type peak with a width of $1T$. If a strongly-coupled medium does not support long-lived excitations, this assumption appears unlikely and the lower limit is more likely to be correct. However, the data cannot definitively prove or disprove this theoretical prejudice. The shear viscosity we obtained in Eq. (34) is close to the hydrodynamic estimate $1 < (4\pi)\eta/s < 2.5$ [61].

TABLE IV. Bulk and shear viscosity fit results for three models, described in the previous section. The errors are statistical only; the difference between different fit models represents a systematic error. In each case, the NLO spectral function at large momentum was used in the fit.

	Model	
Measure	ζ/T^3	η/T^3
M1	0.086(8)	0.77(16)
M2	0.133(10)	1.09(15)
M3	0.303(31)	2.46(54)

In our opinion, there are two pressing tasks to further improve on this work. The first is to find better models for the spectral function's behavior at low to intermediate frequencies $\omega \sim [1-5]T$. This will allow a fitting extraction which makes maximal use of the high-quality data which is now available. The second task is to extend these results to the unquenched case. This is not just a matter of performing much more expensive unquenched simulations. It is also necessary to understand the renormalization of the more-complicated unquenched stress tensor operator at the percent level, which appears to be possible but quite challenging. Some progress in this direction has been made recently by Dalla Brida *et al.* [62], but precision studies including gradient flow do not yet exist. We leave these developments for future work. All data from our calculations, presented in the figures of this paper, can be found in [63].

ACKNOWLEDGMENTS

All authors acknowledge support by the Deutsche Forschungsgemeinschaft (DFG, German Research Foundation) through the CRC-TR 211 "Strong-interaction matter under extreme conditions"—Project No. 315477589—TRR 211. A. F. acknowledges support by the Ministry of Science and Technology Taiwan (MOST) under Grant No. 111-2112-M-A49-018-MY2. The computations in this work were performed on the GPU cluster at Bielefeld University using SIMULATeQCD suite [64,65]. We thank the Bielefeld HPC.NRW team for their support.

APPENDIX A: UNCERTAINTIES OF THE RENORMALIZATION CONSTANTS

In Sec. IV we introduce the renormalization coefficients c_1, c_2 to be used with the traceless and pure-trace stress tensor operators respectively. The coefficient c_2 is determined very accurately from an analytical perturbative series, so there is no need to specify it further than through Eq. (11).

TABLE V. $c_1 \times 10$ at selected flow times in the valid flow time window for all the lattices. The value, and errors, at flow times between the listed values are reliably determined by interpolation.

	$\tau_F T^2$				
$N_s^3 \times N_t$	$64^3 \times 16$	$80^3 \times 20$	$96^3 \times 24$	$120^3 \times 30$	$144^3 \times 36$
0.00158	5.40(6)	5.23(1)	5.22(1)	5.24(2)	5.21(2)
0.00203	5.14(5)	5.00(1)	5.01(1)	5.03(2)	5.01(2)
0.00254	4.93(4)	4.82(1)	4.83(1)	4.85(1)	4.85(2)
0.00310	4.75(3)	4.67(1)	4.68(2)	4.69(2)	4.69(2)
0.00372	4.59(2)	4.52(1)	4.53(2)	4.54(2)	4.55(2)
0.00439	4.45(2)	4.38(1)	4.39(2)	4.40(2)	4.41(2)
0.00513	4.32(2)	4.25(1)	4.27(1)	4.28(2)	4.29(2)
0.00591	4.20(1)	4.14(1)	4.15(1)	4.17(2)	4.17(2)
0.00861	3.88(1)	3.83(1)	3.84(1)	3.87(1)	3.87(1)

The coefficient c_1 depends more strongly on flow depth and lattice spacing, and our nonperturbative determination contains statistical error bars. Therefore, we present tabulated values with errors in Table V for future reference. The errors are an important ingredient in our error analysis and error budget, though the errors in the correlation functions themselves are typically larger.

APPENDIX B: UNCERTAINTIES IN THE TEMPERATURE CORRECTION

In correcting for the slight temperature variation between our lattices, we made the assumption that the temperature dependence in the spectral function is approximately separation-independent. Looking at Fig. 5, it also looks reasonable to assume that the correction is linear in τT. Therefore, we consider this Ansatz, and consider the difference between the two assumptions as a source of systematic uncertainty. This difference is shown for the specific case of the shear channel, the 64×16 lattice, and the flow depth $\tau_F T^2 = 0.00416$ (same as the one used in Fig. 7 and Fig. 13). Note that at this flow time the usable data points must have $\tau T > 0.35$. The figure shows that the difference in these approaches generates an effect which is small compared to, e.g., statistical errors.

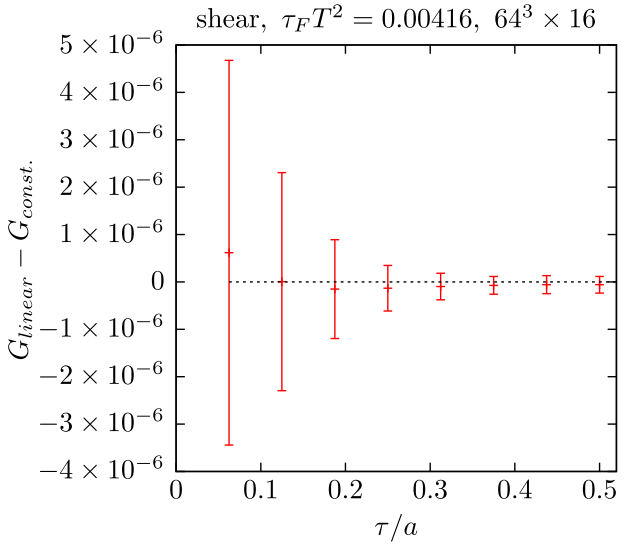

FIG. 13. The difference of correlators obtained in two different ways of treating the slope of the correlators with respect to τT in the temperature correction. Note only data at $\tau T > 0.35$ can be used in later flow-time extrapolation according to the flow-time limitation.

APPENDIX C: THE UNCERTAINTIES IN THE DOUBLE EXTRAPOLATION

The errors in the continuum extrapolation, shown in Fig. 7, are statistical errors arising from the data and from c_1. For the data presented, the bulk-viscous extrapolations are almost flat, but this is not true in general when we consider other flow depths. We tested for the need for a linear term in the extrapolation by repeating the fits assuming no lattice spacing dependence (simply averaging

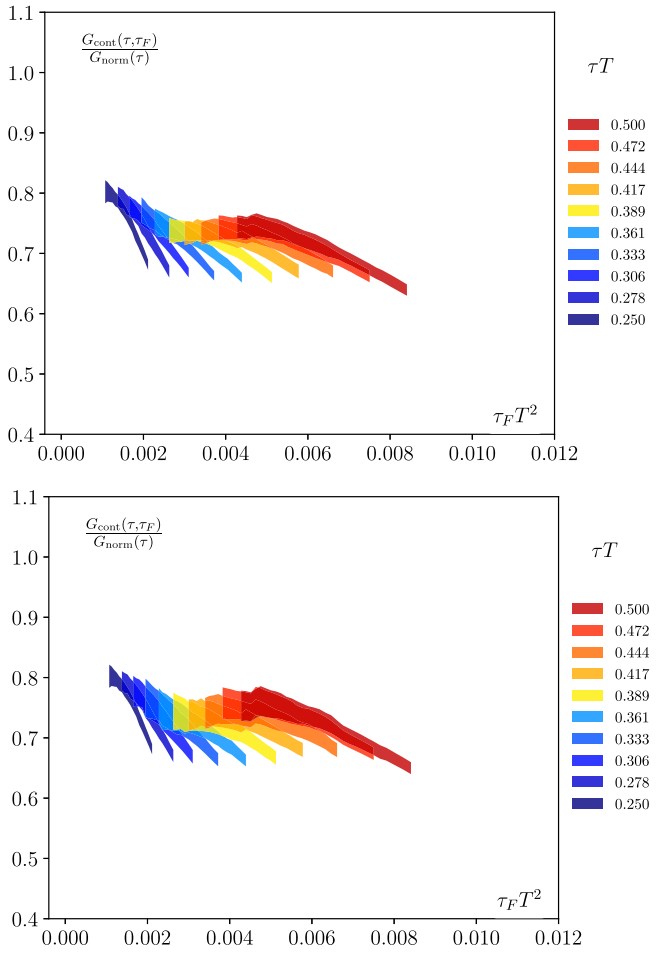

FIG. 14. The difference of continuum-extrapolated correlators in shear channel with (top) and without (bottom) the coarsest lattice.

TABLE VI. Flow-extrapolated results using different kinds of models.

	Measure		
Model	F1	F2	F3
$\delta A[\%]$	0.40	1.84	12.5
χ^2/d.o.f.	14.4	2.14	1.84

data across all lattices). This increases the χ^2/d.o.f. (averaged over all flow times valid for the flow-time extrapolation) from 1.78 to 4.75, showing that linear extrapolation is in fact needed.

We also tried continuum extrapolation excluding the coarsest lattice $64^3 \times 16$, which suffers the most severe discretization effects. We compare the continuum extrapolated correlators in Fig. 14, taking the shear channel as an example. We can see the central values only change very mildly, while the errors increase slightly, as expected. Such changes will affect our estimate of the viscosities by less than the quoted statistical errors.

Next consider the extrapolation to zero flow depth. In the main text we argue that the operator product expansion predicts flow-depth effects which are polynomial in (τ_F/τ^2), at least where this parameter is small. We can then compare three small-flow fit models: a constant, a linear extrapolation, and a quadratic fit,

$$\begin{aligned} &\text{F1}: G(\tau_F/\tau^2) = A, \\ &\text{F2}: G(\tau_F/\tau^2) = A + B\tau_F/\tau^2, \\ &\text{F3}: G(\tau_F/\tau^2) = A + B\tau_F/\tau^2 + C\tau_F^2/\tau^4. \end{aligned} \tag{C1}$$

In Table VI we summarize the flow extrapolated results in the shear channel for the relative error of A in percentage (averaged over $\tau T \in [0.22, 0.5]$) and averaged χ^2/d.o.f. using each of these models, all performed in the same flow-time windows which we use in the main text. It can be seen that fitting the data in Fig. 8 without a linear term leads to a very poor fit, with χ^2/d.o.f. values in the range of [5.5, 28.4]. Adding a τ_F^2 term over-fits the data, dramatically increasing the errors, but is not justified by the very small improvement in χ^2.

APPENDIX D: RELATIVE IMPORTANCE OF STATISTICAL ERROR SOURCES

Statistical errors arise both in our determined c_1, c_2 values (normalization coefficients for the stress tensor) and directly as statistical fluctuations in the measured correlators. To compare the relative importance of these two sources, we have repeated our analysis but leaving out the errors in c_1 (the errors in c_2 are so small that they make no difference). Table VII shows that leaving out the errors in c_1 (middle column) only slightly reduces the final statistical error in the fully extrapolated correlation function. Therefore, the errors in the Euclidean data are, in practice, dominated by statistical errors in the determined correlation functions.

TABLE VII. The (un)importance of the statistical error in c_1. The first column lists separations. The third column is the percent error in the determined fully extrapolated correlation function. The middle column is the error we would find if we neglect the error in c_1.

	τT	
%-error	Case 1	Case 2
0.222	2.30	2.67
0.250	1.41	1.58
0.278	1.73	1.87
0.306	1.48	1.77
0.333	1.56	1.84
0.361	1.64	1.86
0.389	1.50	1.70
0.417	1.75	1.87
0.444	1.69	1.78
0.472	1.69	1.75
0.500	1.51	1.57

[1] K. H. Ackermann *et al.* (STAR Collaboration), Phys. Rev. Lett. **86**, 402 (2001).
[2] S. S. Adler *et al.* (PHENIX Collaboration), Phys. Rev. Lett. **91**, 182301 (2003).
[3] K. Aamodt *et al.* (ALICE Collaboration), Phys. Rev. Lett. **107**, 032301 (2011).
[4] G. Aad *et al.* (ATLAS Collaboration), Phys. Rev. C **90**, 024905 (2014).
[5] J. Adam *et al.* (ALICE Collaboration), Phys. Rev. Lett. **117**, 182301 (2016).
[6] D. Everett *et al.* (JETSCAPE Collaboration), Phys. Rev. C **103**, 054904 (2021).
[7] G. Policastro, D. T. Son, and A. O. Starinets, Phys. Rev. Lett. **87**, 081601 (2001).
[8] P. B. Arnold, G. D. Moore, and L. G. Yaffe, J. High Energy Phys. 11 (2000) 001.
[9] P. B. Arnold, G. D. Moore, and L. G. Yaffe, J. High Energy Phys. 05 (2003) 051.
[10] J. Ghiglieri, G. D. Moore, and D. Teaney, J. High Energy Phys. 03 (2018) 179.

[11] P. B. Arnold, C. Dogan, and G. D. Moore, Phys. Rev. D **74**, 085021 (2006).
[12] A. Nakamura and S. Sakai, Phys. Rev. Lett. **94**, 072305 (2005).
[13] H. B. Meyer, Phys. Rev. D **76**, 101701 (2007).
[14] H. B. Meyer, Phys. Rev. Lett. **100**, 162001 (2008).
[15] N. Astrakhantsev, V. Braguta, and A. Kotov, J. High Energy Phys. 04 (2017) 101.
[16] N. Astrakhantsev, V. Braguta, and A. Kotov, Phys. Rev. D **98**, 054515 (2018).
[17] E. Itou and Y. Nagai, J. High Energy Phys. 07 (2020) 007.
[18] L. Altenkort, A. M. Eller, O. Kaczmarek, L. Mazur, G. D. Moore, and H.-T. Shu, Phys. Rev. D **103**, 014511 (2021).
[19] M. Lüscher and P. Weisz, J. High Energy Phys. 09 (2001) 010.
[20] M. Lüscher, J. High Energy Phys. 08 (2010) 071; 03 (2014) 092.
[21] M. Lüscher, J. High Energy Phys. 04 (2013) 123.
[22] M. Lüscher, Proc. Sci. LATTICE2010 (**2010**) 015 [arXiv: 1009.5877].
[23] R. Narayanan and H. Neuberger, J. High Energy Phys. 03 (2006) 064.
[24] L. Altenkort, A. M. Eller, O. Kaczmarek, L. Mazur, G. D. Moore, and H. T. Shu, Phys. Rev. D **105**, 094505 (2022).
[25] H. Suzuki, Prog. Theor. Exp. Phys. **2013**, 083B03 (2013); **2015**, 079201(E) (2015).
[26] H. Suzuki and H. Takaura, Prog. Theor. Exp. Phys. **2021**, 073B02 (2021).
[27] R. V. Harlander, Y. Kluth, and F. Lange, Eur. Phys. J. C **78**, 944 (2018); **79**, 858(E) (2019).
[28] T. Iritani, M. Kitazawa, H. Suzuki, and H. Takaura, Prog. Theor. Exp. Phys. **2019**, 023B02 (2019).
[29] R. V. Harlander and T. Neumann, J. High Energy Phys. 06 (2016) 161.
[30] L. Giusti and M. Pepe, Phys. Rev. D **91**, 114504 (2015).
[31] M. Lüscher and P. Weisz, J. High Energy Phys. 02 (2011) 051.
[32] L. Del Debbio, A. Patella, and A. Rago, J. High Energy Phys. 11 (2013) 212.
[33] R. Sommer, Nucl. Phys. **B411**, 839 (1994).
[34] A. Francis, O. Kaczmarek, M. Laine, T. Neuhaus, and H. Ohno, Phys. Rev. D **91**, 096002 (2015).
[35] Y. Burnier, H. T. Ding, O. Kaczmarek, A. L. Kruse, M. Laine, H. Ohno, and H. Sandmeyer, J. High Energy Phys. 11 (2017) 206.
[36] A. Ramos and S. Sint, Eur. Phys. J. C **76**, 15 (2016).
[37] P. Fritzsch and A. Ramos, J. High Energy Phys. 10 (2013) 008.
[38] L. Giusti and M. Pepe, Phys. Lett. B **769**, 385 (2017).
[39] A. M. Eller and G. D. Moore, Phys. Rev. D **97**, 114507 (2018).
[40] Z. Fodor, K. Holland, J. Kuti, D. Nogradi, and C. H. Wong, J. High Energy Phys. 11 (2012) 007.
[41] A. Hasenfratz and O. Witzel, Phys. Rev. D **101**, 034514 (2020).
[42] S. Caracciolo, G. Curci, P. Menotti, and A. Pelissetto, Ann. Phys. (N.Y.) **197**, 119 (1990).
[43] S. Caracciolo, P. Menotti, and A. Pelissetto, Nucl. Phys. **B375**, 195 (1992).
[44] A. Francis, O. Kaczmarek, M. Laine, T. Neuhaus, and H. Ohno, Phys. Rev. D **92**, 116003 (2015).
[45] H.-T. Ding, O. Kaczmarek, A.-L. Lorenz, H. Ohno, H. Sandmeyer, and H.-T. Shu, Phys. Rev. D **104**, 114508 (2021).
[46] V. Gimenez, L. Giusti, S. Guerriero, V. Lubicz, G. Martinelli, S. Petrarca, J. Reyes, B. Taglienti, and E. Trevigne, Phys. Lett. B **598**, 227 (2004).
[47] H. B. Meyer, J. High Energy Phys. 06 (2009) 077.
[48] L. Altenkort, A. M. Eller, O. Kaczmarek, L. Mazur, G. D. Moore, and H.-T. Shu, Phys. Rev. D **103**, 114513 (2021).
[49] H. Makino and H. Suzuki, Prog. Theor. Exp. Phys. **2014**, 063B02 (2014); **2015**, 079202(E) (2015).
[50] G. Backus and F. Gilbert, Geophys. J. R. Astron. Soc. **16**, 169 (1968).
[51] J. S. Hadamard, *Lectures on Cauchy's Problem in Linear Partial Differential Equations* (Yale University Press, New Haven, 1923), Vol. 18.
[52] Y. Zhu and A. Vuorinen, J. High Energy Phys. 03 (2013) 002.
[53] K. Kajantie, M. Laine, K. Rummukainen, and M. E. Shaposhnikov, Nucl. Phys. **B503**, 357 (1997).
[54] A. Vuorinen and Y. Zhu, J. High Energy Phys. 03 (2015) 138.
[55] M. Laine, A. Vuorinen, and Y. Zhu, J. High Energy Phys. 09 (2011) 084.
[56] B. B. Brandt, A. Francis, H. B. Meyer, and D. Robaina, Phys. Rev. D **92**, 094510 (2015).
[57] B. B. Brandt, A. Francis, B. Jäger, and H. B. Meyer, Phys. Rev. D **93**, 054510 (2016).
[58] M. Hansen, A. Lupo, and N. Tantalo, Phys. Rev. D **99**, 094508 (2019).
[59] V. A. Morozov, *Methods for Solving Incorrectly Posed Problems* (Springer, Berlin, 1984).
[60] G. Aarts and J. M. Martinez Resco, Nucl. Phys. **B726**, 93 (2005).
[61] H. Song, S. A. Bass, U. Heinz, T. Hirano, and C. Shen, Phys. Rev. Lett. **106**, 192301 (2011); **109**, 139904(E) (2012).
[62] M. Dalla Brida, L. Giusti, and M. Pepe, J. High Energy Phys. 04 (2020) 043.
[63] L. Altenkort, A. M. Eller, A. Francis, O. Kaczmarek, L. Mazur, G. D. Moore, and H. - T. Shu, Data publication: Viscosity of pure-glue QCD from the lattice (2023), 10.4119/unibi/2980224.
[64] L. Altenkort, D. Bollweg, D. A. Clarke, O. Kaczmarek, L. Mazur, C. Schmidt, P. Scior, and H.-T. Shu, Proc. Sci. LATTICE2021 (**2022**) 196 [arXiv:2111.10354].
[65] L. Mazur, Ph.D. thesis, Bielefeld University (2021).